Progress In Electromagnetics Research, PIER 44, 197–215, 2004

THE PROPER CURRENT SPECTRA OF AN OPEN INTEGRATED MICROSTRIP WAVEGUIDE

J.-S. Lee

University of Illinois at Urbana-Champaign
Department of Electrical and Computer Engineering
464 Everitt Laboratory
1406 W. Green Str., Urbana, IL 61801, USA

D. P. Nyquist

Michigan State University
Department of Electrical and Computer Engineering
C132 Engineering Research Complex
MI, USA

Abstract—Continuous current spectrum of an integrated open waveguide structure is identified as the branch cut contribution to singularity expansion of those currents in the complex axial transform plane. Those singularities in that plane include poles associated with the guiding structure and branch points contributed by layered background environments. The manner in which singularities in background environments manifest themselves as branch points in the complex axial transform plane is reviewed.

Based on spectral integral equation formulation, approximate and analytical expression for spatial microstrip current is obtained. That approximation is based on Maxwellian distribution for the transverse current profile. This result is the representation of currents in terms of proper propagation mode spectrum. During the integration around branch cuts, singularities in the transverse transform plane migrate in a complicated manner. The trajectories of this migration are identified and suitably accommodated during the real axis integration in that plane. This overall procedure leads to a decomposition of the total currents into bound modes and continuous spectrum contributions. This representation is validated by real axis integration in the axial transform plane. The quasi TEM characteristic impedance of bound mode is calculated and validated by comparison with well-known empirical formula.

1. INTRODUCTION AND GEOMETRICAL CONFIGURATION

The existence of leaky modes on the integrated open waveguide structure has recently received considerable attention [1–14]. However, the proper continuous and discrete spectrum currents of the integrated open microstrip waveguide have been until recently neither conceptualized nor quantified adequately. That spectrum can be identified as the branch cut contribution to a singularity expansion of those currents in the complex axial transform plane (ζ-plane). It is recognized that singularities in that plane include poles associated with the guiding structure and branch points contributed by layered background environments. The manner in which singularities in background environments manifest themselves as branch points in the complex ζ-plane is reviewed.

Based on a spectral EFIE (electric field integral equation) formulation [15–17], both approximate and analytical expressions for the spectral microstrip current are obtained. A δ-gap field feed model is exploited as an excitatory source [18–21]. It is noted that the current approximation is based on the Maxwellian distribution for the transverse current profile. Microstrip currents are recovered from the spectral representation by integration contour deformation on the top sheet of the complex ζ-plane. As a result, microstrip currents are obtained in terms of the proper propagation mode spectrum. That spectrum consists of bound propagation modes associated with pole singularities and a continuous spectrum [22, 23] which is associated with integration around branch cuts contributed by background layer environments. During integration around the branch cuts, singularities in the complex transverse transform plane (ξ-plane) tend to migrate in a complicated manner. The trajectories of ξ-plane migration are identified and suitably accommodated during the real axis integration in the complex ξ-plane. This overall procedure leads to a decomposition of the total currents into bound mode

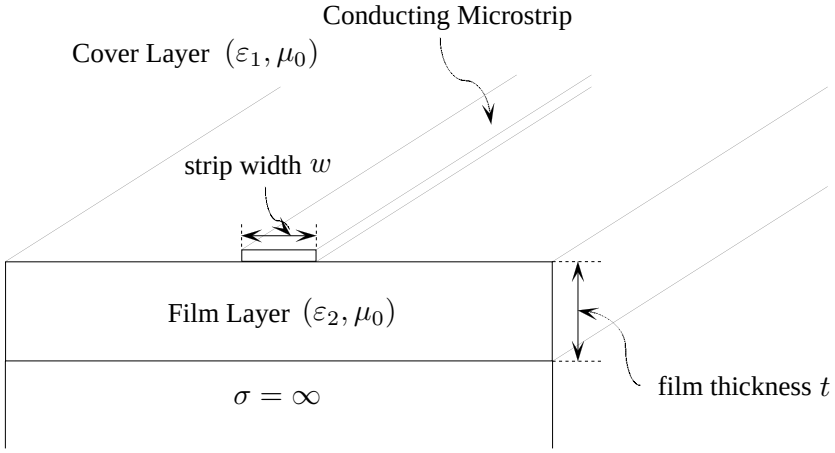

Figure 1. Geometrical configuration of open microstrip structure immersed in layered background environment.

and continuous spectrum contributions. The result is numerically validated by real axis integration in the complex ζ-plane. The quasi TEM characteristic impedance of bound modes associated with pole singularities is calculated and is validated by comparison with well-known empirical formulas [24].

Extensive numerical results are obtained, which can compare bound mode and continuous spectrum contributions to microstrip currents. It is recognized that currents are dominated by bound propagation modes. Physically, it is acceptable since the microstrip current is directly associated with the conducting microstrip rather than the background layer environment. Even if the continuous current spectrum is maximal near the feed point and decays rapidly with axial distance from the feed, it contributes negligibly to the total spectrum since the dominant contribution comes from the discrete current spectrum contributed by the bound propagation mode.

The geometrical configuration of integrated microstrip waveguide immersed in a planar-layered background environment is depicted in Fig. 1 and its cross-sectional view is also depicted in Fig. 2. Each of the planar layers is assumed to be non-magnetic, isotropic and homogeneous with complex permittivity ε_l, $l = 1, 2, 3$ for the cover, film, and substrate layers with $\varepsilon_3 \to -j\infty$ or $\sigma \to \infty$. The guiding structure is embedded in the cover layer adjacent to the cover/film interface.

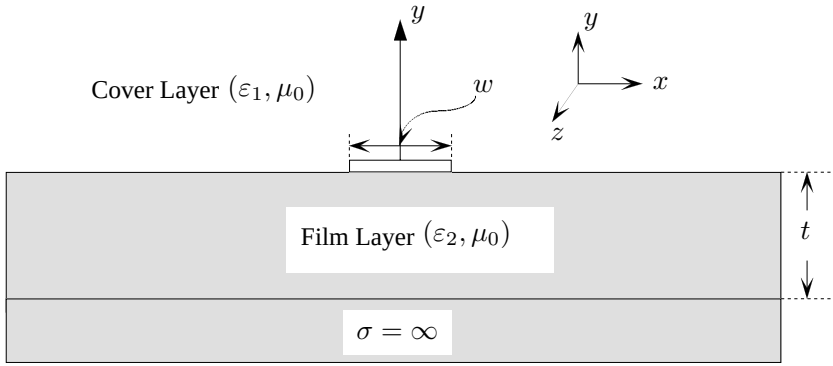

Figure 2. Cross-sectional view of immersed microstrip structure.

2. CONTINUOUS SPECTRUM CURRENT

The microstrip current is formulated under the assumption of Maxwellian transverse current distribution in [25] and it will not be repeated here. The current is given by [26]

$$J_z(z) = \int_{-\infty}^{\infty} \frac{\tilde{L}_g(\zeta)}{\displaystyle\int_{-\infty}^{\infty} \tilde{\eta}^2(\xi) \left[\frac{j\eta}{k_1}\tilde{\tilde{C}}_{zz}(\xi,\zeta)\right] d\xi} e^{j\zeta z} d\zeta \tag{1}$$

The parameters $\tilde{L}_g(\zeta)$, $\tilde{\eta}(\xi)$ and $\tilde{\tilde{C}}_{zz}(\xi,\zeta)$ are given by

$$\begin{aligned}
\tilde{L}_g(\zeta) &= e^{-(\zeta d)^2}/2 \\
\tilde{\eta}(\xi) &= \begin{cases} J_0(\xi w/2) & \cdots \ w/t < 2 \\ \sin c(\xi w/2) & \cdots \ w/t \geq 2 \end{cases} \\
\tilde{\tilde{C}}_{zz}(\xi,\zeta) &= \frac{(k_1^2 - \zeta^2)}{Z^h(\lambda)} + \frac{\zeta^2 p_1(\lambda)\,(N_{21}^2 - 1)}{Z^h(\lambda) Z^e(\lambda)} \\
Z^h(\lambda) &= p_1(\lambda) + p_2(\lambda)\coth[p_2(\lambda)t] \\
Z^e(\lambda) &= N_{21}^2 p_1(\lambda) + p_2(\lambda)\tanh[p_2(\lambda)t] \\
\lambda^2 &= \xi^2 + \zeta^2, \quad N_{21}^2 = (n_2/n_1)^2
\end{aligned} \tag{2}$$

where d, w and t denote the effective gap width, microstrip width and film layer thickness respectively. It is also noted that ξ and ζ are transverse and longitudinal transform variables respectively. As discussed in [27], $p_l(\lambda) = \sqrt{\lambda^2 - k_l^2}\,(l = 1, 2)$ yield branch point

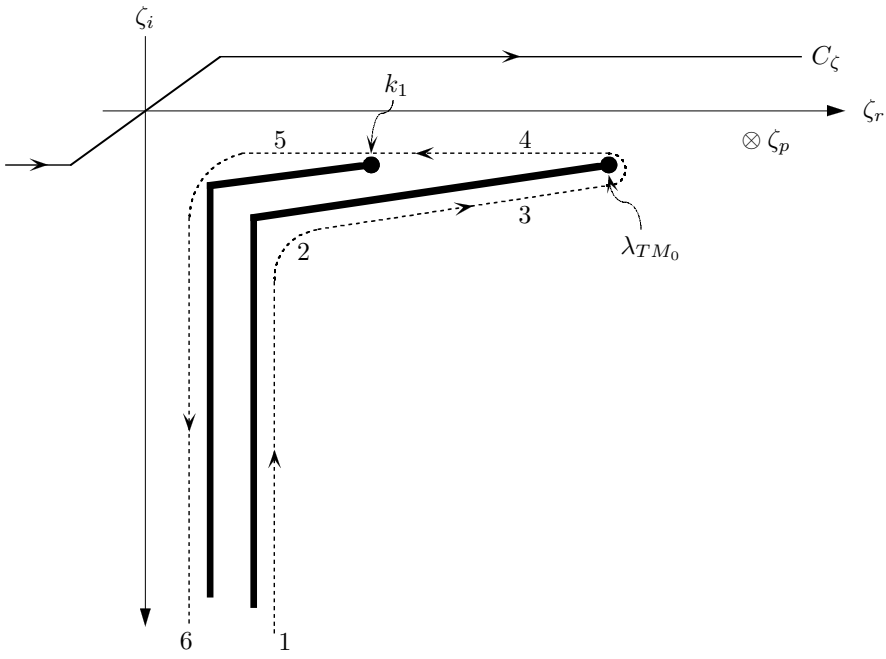

Figure 3. Singularities in the complex ζ-plane contributed by the planar-layered background environment. The branch points $\lambda_s = \pm k_1$ to the branch points $\pm k_1$ mapping and the poles $\lambda_s = \pm\lambda_{TM_0}$ to the branch points $\pm\lambda_{TM_0}$ mapping in the low low-loss limit.

singularities at $\lambda = \pm k_l$. It is observed that the branch points contributed by inner layers are removable [28] but those contributed by most-outer layers are non-removable.

Pole singularities of $\tilde{\tilde{C}}_{zz}(\xi, \zeta)$ contribute simple-pole singularities associated with the planar-layered background environment. Then, $Z^h(\lambda) = 0$ leads to simple poles at $\lambda = \pm\lambda_p$ associated with TE-odd surface waves and $Z^e(\lambda) = 0$ leads to simple poles associated with TM-even surface waves.

Hence, complex λ-plane singularities of the integral representation for the microstrip current consist of branch points at $\lambda = \pm k_1$ and poles $\lambda = \pm\lambda_p$. Since $\lambda_s^2 = \xi_s^2 + \zeta^2$ (conventionally, λ_s and ξ_s denotes λ- and ξ-plane singularities),

$$\begin{aligned} \pm\xi_{k_1} &= \mp j\sqrt{\zeta - \lambda_s}\sqrt{\zeta + \lambda_s} = \mp j\sqrt{\zeta - k_1}\sqrt{\zeta + k_1} \\ \pm\xi_{TM_0} &= \mp j\sqrt{\zeta - \lambda_s}\sqrt{\zeta + \lambda_s} = \mp j\sqrt{\zeta - \lambda_{TM_0}}\sqrt{\zeta + \lambda_{TM_0}} \end{aligned} \tag{3}$$

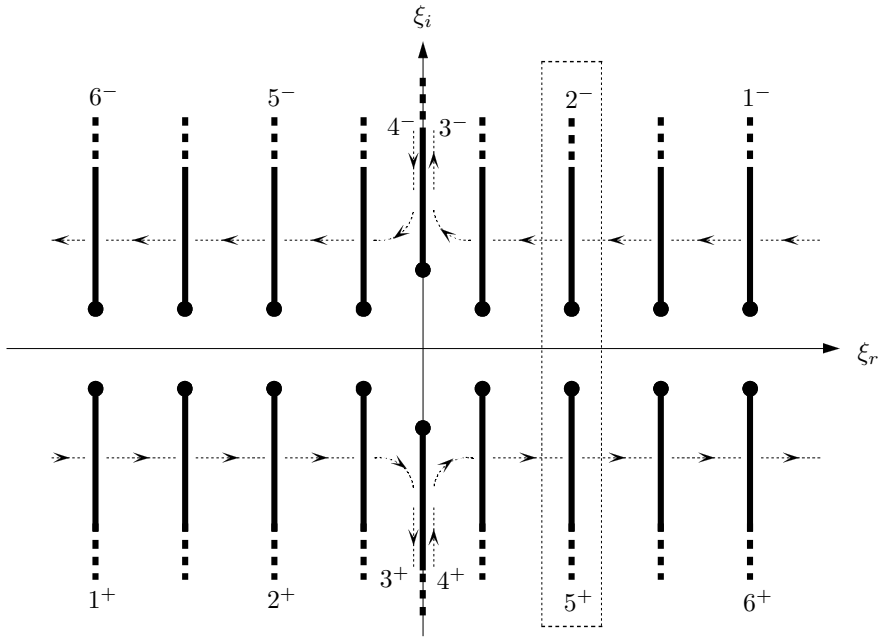

Figure 4. Migration of complex transverse transform plane (complex ξ-plane) branch-point singularities $\pm\xi_{k_1}$ in conjunction with changing spatial-frequency ζ along branch cuts associated with a logarithmic type branch point k_1 and a square-root type branch point λ_{TM_0} in the complex ζ-plane in the low-loss limit.

which clearly implicates the branch points at $\zeta = \pm\lambda_s$ in the complex ζ-plane with $\lambda_p = \lambda_{TM_0}$ being the fundamental proper surface-wave mode as depicted in Fig. 3. It is assumed that $k_0 t$ is sufficiently small that the TM_0 pole is the only mode on the top sheet of the complex λ-plane. Singularities associated with the background layer environment consist of branch points in the complex ζ-plane. The proper continuous spectrum is contributed by detouring about logarithmic and square-root type branch cuts arising from the k_1 branch point and the proper background pole λ_{TM_0} as depicted in Fig. 3. Then, as evident from Eqn. (3), branch point and surface-wave pole singularities in the complex ξ-plane migrate in conjunction with changing spatial-frequency ζ along branch cuts associated with a logarithmic type branch point k_1 and a square-root type branch point k_{TM_0} in the complex ζ-plane as depicted in Figs. 4 and 6 respectively. For a point along a branch cut contour in the complex ζ-plane, Re$\{\xi\}$-axis inversion contour integration is implemented for its corresponding

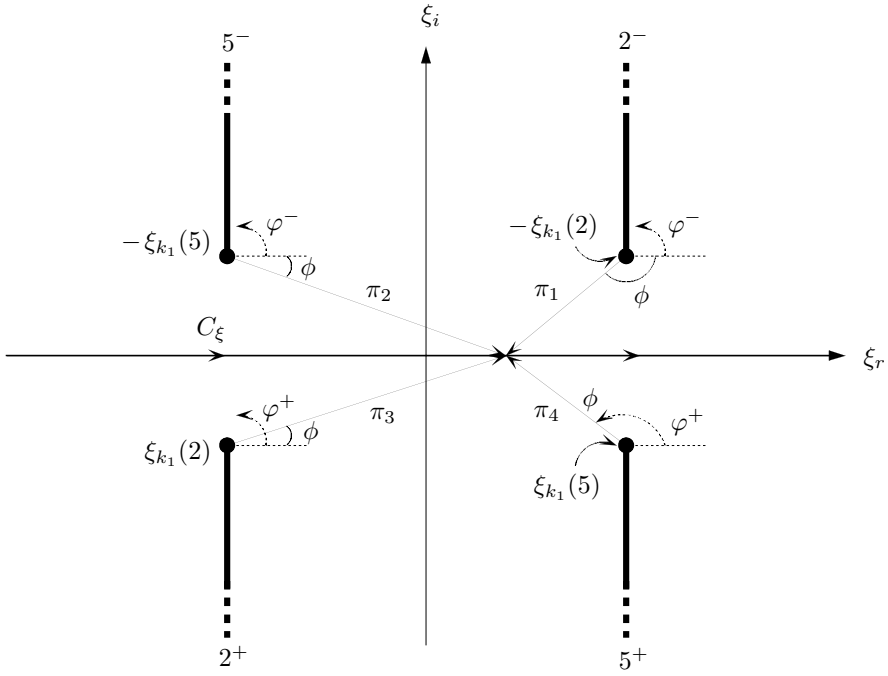

Figure 5. Complex-phasor diagram for branch-point singularities $\pm\xi_{k_1}$ in the complex ξ-plane for points 2 and 5 in the complex ζ-plane in Fig. 3 and evolution of C_ξ.

branch-point singularities $\pm\xi_{k_1}$. The integration detour about branch cuts from a point 4 to a point 6 is in an opposite sense to that from a point 1 to a point 3 as depicted in Fig. 3. Thus, the corresponding $\mathrm{Re}\{\xi\}$-axis inversion contour C_ξ's are also in an opposite sense to each other as depicted in Fig. 4, but their integral contributions are not annulled by each other since $p_1(\xi,\zeta)$ takes different values along them on the top sheet of the complex ξ-plane and must be evaluated with respect to different branch-point singularities in the complex ξ-plane for corresponding different ζ's in the complex ζ-plane. For example, ξ_{k_1} (2) and $-\xi_{k_1}$ (2) in Fig. 5 imply positive and negative branch-point singularities ξ_{k_1} and $-\xi_{k_1}$ respectively for a point 2 in Fig. 3.

$$p_1(\xi,\zeta) = \sqrt{\xi^2+\zeta^2-k_1^2} = \sqrt{\xi+\xi_{k_1}}\sqrt{\xi-\xi_{k_1}} \tag{4}$$

Regarding ξ_{k_1} as a fourth-quadrant singularity leads to

$$\xi_{k_1} = -j\sqrt{\zeta-k_1}\sqrt{\zeta+k_1} \tag{5}$$

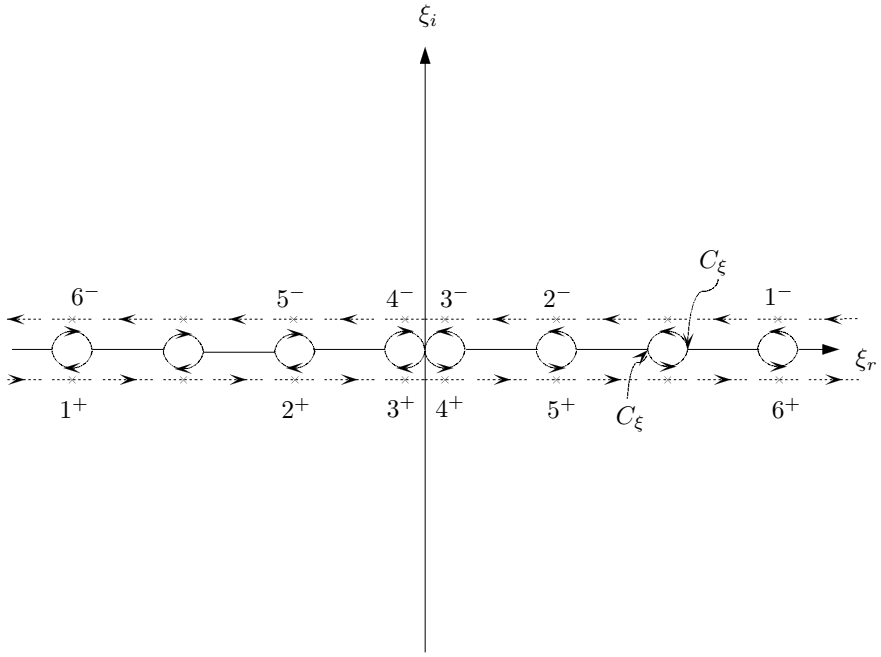

Figure 6. Migration of complex transverse transform plane (complex ξ-plane) surface-wave pole singularities $\pm\xi_{TM_0}$ in conjunction with changing spatial-frequency ζ along branch cuts associated with a logarithmic type branch point k_1 and a square-root type branch point λ_{TM_0} in the complex ζ-plane in the low-loss limit.

For π_1 in Fig. 5,

$$\pi_1 = \xi + \xi_{k_1}(2) = \gamma_1 e^{j\varphi^-} \tag{6}$$

$$\gamma_1 = \sqrt{\left[\mathrm{Re}\left\{\xi + \xi_{k_1}(2)\right\}\right]^2 + \left[\mathrm{Im}\left\{\xi + \xi_{k_1}(2)\right\}\right]^2}$$

$$\varphi^- = -\phi$$

$$= -\tan^{-1}\left(\frac{\mathrm{Im}\{\xi + \xi_{k_1}(2)\}}{\mathrm{Re}\{\xi + \xi_{k_1}(2)\}}\right) + \frac{\pi}{2}\left(\mathrm{sgn}[\mathrm{Re}\{\xi + \xi_{k_1}(2)\}] - 1\right) \tag{7}$$

where

$$\mathrm{sgn}[\mathrm{Re}\{\xi + \xi_{k_1}(2)\}] = \begin{cases} 1 \cdots \mathrm{Re}\{\xi + \xi_{k_1}(2)\} > 0 \\ -1 \cdots \mathrm{Re}\{\xi + \xi_{k_1}(2)\} < 0 \end{cases}$$

Similar analysis can be implemented for π_2, π_3 and π_4. Therefore, for

a point 2 in Fig. 3, $p_1(\xi,\zeta)$ is defined by

$$p_1(\xi,\zeta) = \sqrt{\gamma_1\gamma_3}e^{j(\varphi^- + \varphi^+)/2} \tag{8}$$

where γ_1, φ^- are determined by Eqn. (7) and γ_3, φ^+ can be obtained for complex phasor analysis for π_3. Thus, throughout the integration detour about branch cuts from a point 1 to 6 in Fig. 3, the corresponding overall procedure for Re$\{\xi\}$-axis inversion contour C_ξ's leads to

$$\int_{\sum_{m=1}^{6} C_\xi(m)} (\cdots)d\xi = \int_{\sum_{m=1}^{3} C_\xi(m)} (\cdots)d\xi - \int_{\sum_{m=4}^{6} C_\xi(m)} (\cdots)d\xi \tag{9}$$

where $C_\xi(m)$ indicates Re$\{\xi\}$-axis inversion contour for a corresponding point m in Fig. 3. Then, Eqn. (9) implicates Re$\{\xi\}$-axis inversion contour integral contribution excluding surface-wave pole singularities on Re$\{\xi\}$-axis defined by Eqn. (3).

As evident from Eqn. (3), in addition to branch-point singularities $\pm\xi_{k_1}$, there exist surface-wave pole singularities $\pm\xi_{TM_0}$ in the complex ξ-plane for corresponding points on the branch-cut contour in Fig. 3. As the integration contour detours from a point 1 to a point 6 about branch cuts in the complex ζ-plane as depicted in Fig. 3, one of surface-wave pole singularities, ξ_{TM_0}, in the complex ξ-plane, migrates from $-\infty$ to ∞ on Re$\{\xi\}$-axis in the low-loss limit as depicted in Fig. 6. The symbol $\times$ denotes the surface-wave pole singularity in the complex ξ-plane for a corresponding point on branch cuts in the complex ζ-plane. The superscript + denotes the positive surface-wave pole singularity ξ_{TM_0} and the number does its corresponding position on the branch-cut contour in the complex ζ-plane. For example, 1^+ implies that a point 1 in the complex ζ-plane as depicted in Fig. 3 maps into a positive surface-wave pole singularity ξ_{TM_0} in the complex ξ-plane. Similarly, the negative surface-wave pole singularity, $-\xi_{TM_0}$, migrates exactly conversely from ∞ to $-\infty$ on Re$\{\xi\}$-axis as depicted in Fig. 6. Therefore, there is a continuum of surface-wave pole singularities in the complex ξ-plane for corresponding points on the branch-cut contour in the complex ζ-plane. The location of a surface-wave pole singularity is a little exaggerated for clarity in Fig. 6. In the low-loss limit, a positive surface-wave pole singularity ξ_{TM_0} approaches infinitesimally close to Re$\{\xi\}$-axis from the below as depicted in Fig. 6 since it is necessary that Im$\{\xi_{TM_0}\} < 0$ to satisfy the radiation condition. Conversely, a negative surface-wave pole singularity $-\xi_{TM_0}$ approaches infinitesimally close to Re$\{\xi\}$-axis from the above in Fig. 6 since it is necessary that Im$\{-\xi_{TM_0}\} > 0$. If physical continuity of the surface-wave is to be maintained during Re$\{\xi\}$-axis inversion contour

integration, Re$\{\xi\}$-axis inversion contour must remain disposed above the positive surface-wave pole singularity ξ_{TM_0}. Then, the half residue contributed by ξ_{TM_0} leads to a surface-wave contribution. From a point 1 to a point 3 about the branch cut in the complex ζ-plane as depicted in Fig. 3, the corresponding positive surface-wave pole singularities $1^+, 2^+, 3^+$ in Fig. 6 are in a clockwise sense however from a point 4 to a point 6 about the branch cut in Fig. 3, the corresponding positive surface-wave pole singularities $4^+, 5^+, 6^+$ in Fig. 6 are in a counter-clockwise sense since the branch cut integration contour from a point 4 to a point 6 in Fig. 3 is in an opposite sense to that from a point 1 to a point 3. Conversely, Re$\{\xi\}$-axis inversion contour must remain disposed below the negative surface-wave pole singularity $-\xi_{TM_0}$ and the half residue contributed by $-\xi_{TM_0}$ leads to a surface-wave contribution. From a point 1 to a point 3 about the branch cut in the complex ζ-plane as depicted in Fig. 3, the corresponding negative surface-wave pole singularities $1^-, 2^-, 3^-$ as depicted in Fig. 6 are in a counter-clockwise sense however from a point 4 to a point 6 about the branch cut in Fig. 3, the corresponding negative surface-wave pole singularities $4^-, 5^-, 6^-$ as depicted in Fig. 6 are in a clockwise sense. Hence the overall procedure leads to a full residue contribution for two corresponding points on the branch cut contour in Fig. 3. More importantly, since all the residues on a positive Re$\{\xi\}$-axis are in a counter-clockwise sense and those on a negative Re$\{\xi\}$-axis in a clockwise sense, the overall residue contribution will not be annulled.

Hence, both branch-point and surface-wave pole singularities contribute to the proper continuous spectrum since the branch cut contour never violates the branch-cut as depicted in Fig. 3.

3. THE CHARACTERISTIC IMPEDANCE

As is evident from Eqn. (1), the discrete spectrum or the bound-mode spectrum is associated with bound- or guided-mode pole singularities ζ_p in the complex ζ-plane in Fig. 3 determined by

$$\int_{-\infty}^{\infty} \tilde{\eta}^2(\xi) \left[\frac{j\eta_1}{k_1} \tilde{\tilde{C}}_{zz}(\xi, \zeta_p) \right] d\xi = 0 \tag{10}$$

It is noted that the characteristic impedance of the microstrip waveguide is not unique since it supports quasi TEM-modes. However, a meaningful characteristic impedance can be calculated by exploiting the discrete (bound-mode) spectrum current. The discrete current I_D is propagating longitudinally with a voltage V. It is important to observe that voltage V can be decomposed into $V/2$ at $z = 0$ since

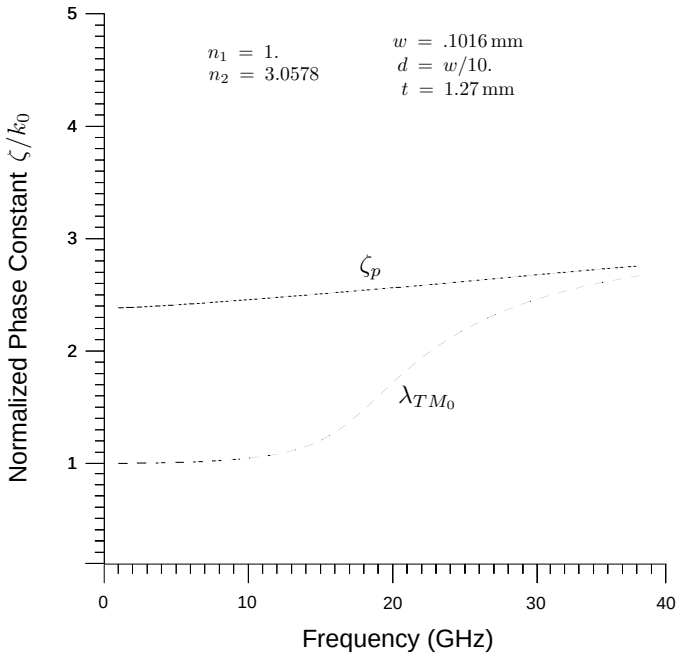

Figure 7. The dispersion of the fundamental surface-wave pole singularity λ_{TM_0} and the bound or guided-mode pole singularity ζ_p through operating frequency ranges.

infinitesimally equally and oppositely separated discrete currents can flow at $z = 0$ [29]. Then, the characteristic impedance Z_c is derived by

$$Z_c = \frac{V/2}{I_D(z=0)} = \frac{V}{2I_D(z=0)} \tag{11}$$

where $I_D(z = 0)$ is the discrete (bound-mode) current at $z = 0$. The fundamental proper surface-wave mode λ_{TM_0} and the bound-mode pole singularity ζ_p are dispersed through operating frequency ranges (1∼38 GHz) as depicted in Fig. 7. The characteristic impedance Z_c of the microstrip waveguide excited by a δ-gap is depicted in Fig. 8 and compared with the well-known empirical formula [24].

4. NUMERICAL RESULTS

Numerical results are obtained using the integrated microstrip configuration with

$$\text{microstrip width}: \qquad w = .1016\,\text{mm} \Rightarrow w/\lambda_0 = .0051$$

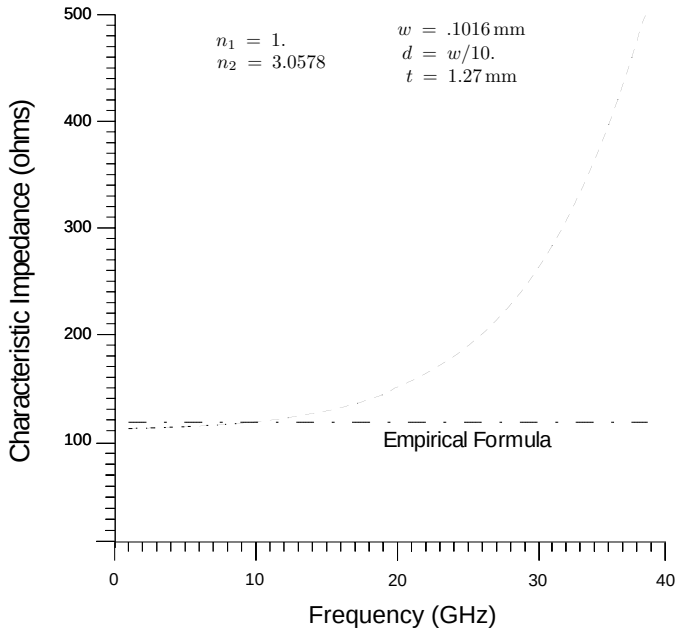

Figure 8. The characteristic impedance of the microstrip waveguide calculated by the longitudinal discrete or bound-mode current spectrum through operating frequency ranges.

$$\begin{aligned} \text{effective gap width}: &\quad d = w/10\,\text{mm} \Rightarrow d/\lambda_0 = (w/\lambda_0)/10 \\ \text{film thickness}: &\quad t = 1.27\,\text{mm} \Rightarrow t/\lambda_0 = .06 \\ \text{operating frequency}: &\quad f = 15\,\text{GHz} \end{aligned}$$

The microstrip current is composed of the continuous spectrum current contributed by the background layer environment (branch points) and the discrete spectrum current contributed by the guiding structure (poles). As depicted in Fig. 9, the microstrip current is dominated by the discrete spectrum current rather than the continuous spectrum current. It is noted that physically, the microstrip current is associated with the guiding structure rather than the background layer environment. Furthermore, the total microstrip current spectrum can be validated by $\text{Re}\{\zeta\}$-axis inversion contour integration as depicted in Figs. 10 and 11. The corresponding ξ-singularity migration will not be repeated here. Fig. 12 depicts the microstrip current amplitude profile with various electrical strip widths. The continuous (I_C) and discrete (I_D) spectrum current amplitude-ratio with various electrical strip widths is depicted in Fig. 13. Fig. 14 depicts the continuous (I_C)

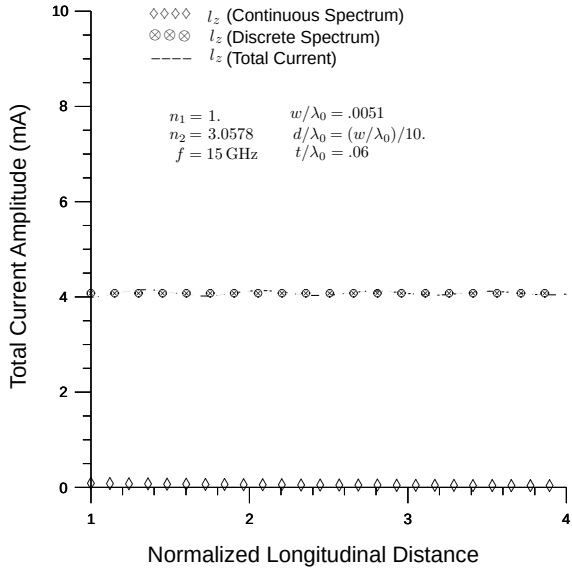

Figure 9. Total microstrip current amplitude profile contributed by the continuous spectrum current and the discrete spectrum current.

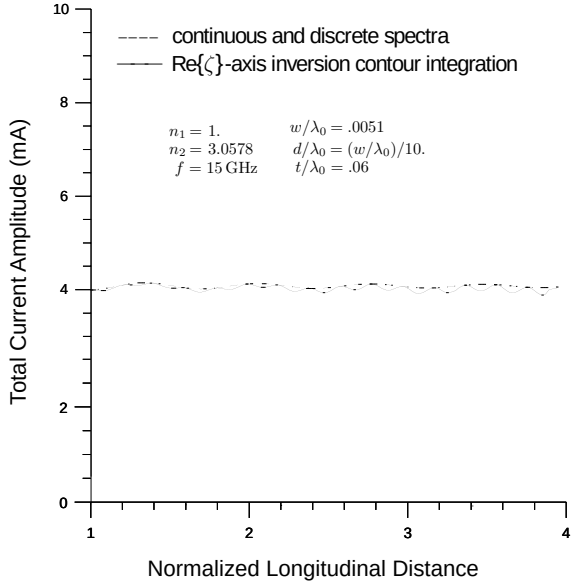

Figure 10. Re{ζ}-axis inversion contour validation of microstrip current amplitude profile contributed by the continuous spectrum current and the discrete spectrum current.

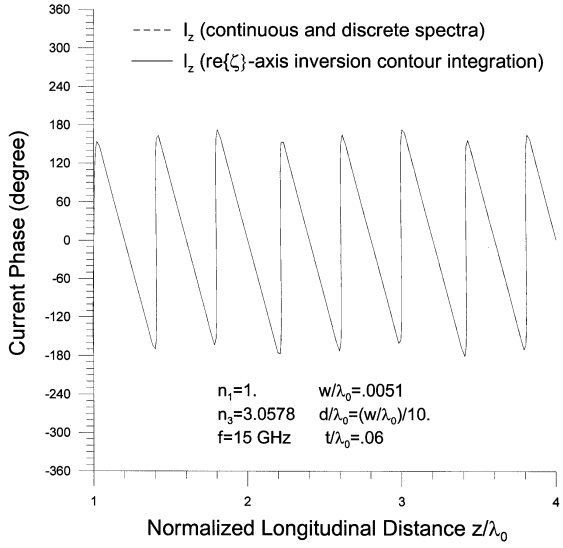

Figure 11. Re{ζ}-axis inversion contour validation of microstrip current phase profile contributed by the continuous spectrum current and the discrete spectrum current.

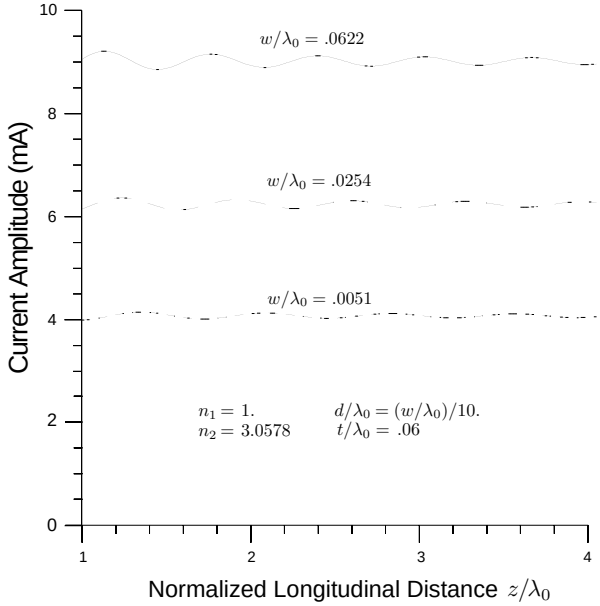

Figure 12. Microstrip current amplitude profile with various electrical strip widths.

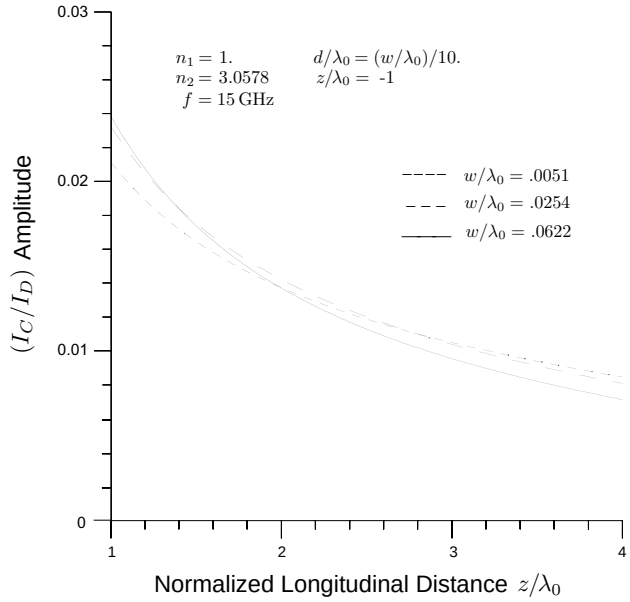

Figure 13. Microstrip continuous and discrete spectrum current amplitude-ratio with various electrical strip widths.

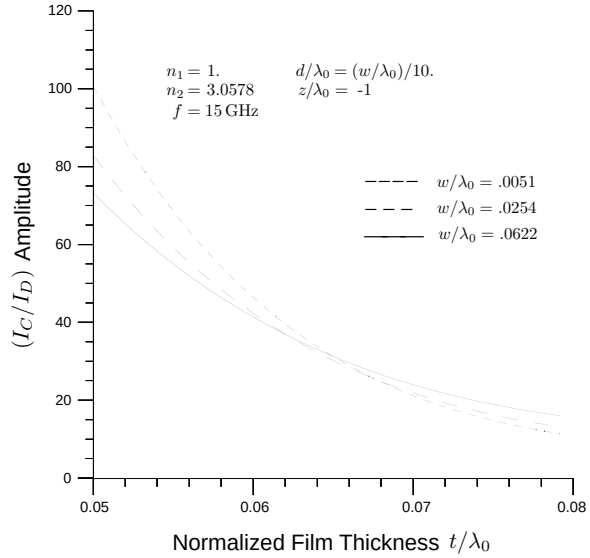

Figure 14. Microstrip continuous and discrete spectrum current amplitude-ratio versus electrical film thickness with various electrical strip widths.

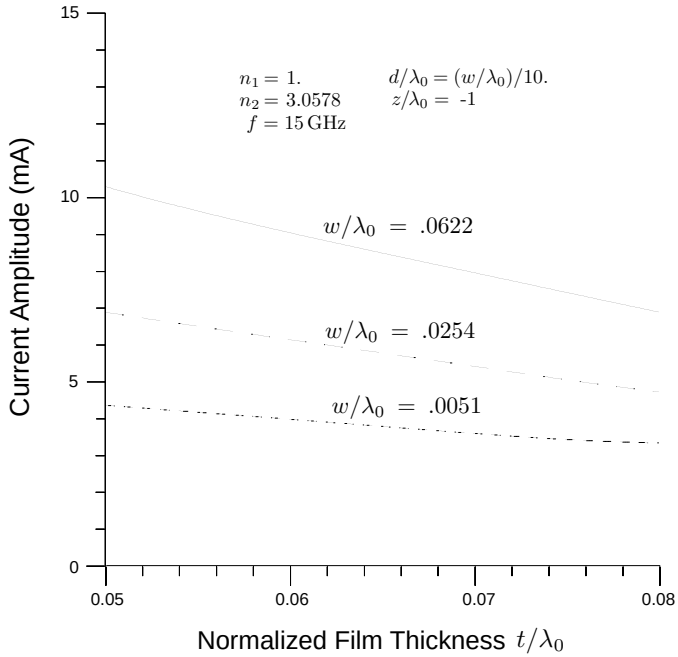

Figure 15. Microstrip current amplitude versus electrical film thickness with electrical strip widths.

and discrete (I_D) spectrum current amplitude-ratio versus electrical film thickness with various electrical strip widths. Finally, Fig. 15 depicts the microstrip current amplitude versus electrical film thickness with various electrical strip widths.

5. CONCLUSION

It is observed that singularities in the complex ζ-plane include poles associated with the guiding structure and branch points contributed by the layered background environment. Singularities associated with the background layer environment manifest themselves as branch points in the complex ζ-plane. The continuous spectrum current is contributed by the integration contour about branch cuts associated with those branch points. The discrete spectrum current is contributed by residues at pole singularities associated with the guiding structure. The characteristic impedance of the microstrip was obtained using the discrete- or bound-mode spectrum current and was validated by comparison with a well-known empirical formula.

Microstrip current is composed of the continuous spectrum current and the discrete spectrum current. Numerically it is observed that the total microstrip current is dominated by the discrete spectrum current rather than that of the continuous spectrum. The microstrip current was validated by comparison with $\mathrm{Re}\{\zeta\}$-axis inversion contour integration.

Based upon the microstrip current and the proposed methodology, the fields in the background layer environments will be presented in a forthcoming paper.

REFERENCES

1. Oliner, A. A., "Leakage from higher modes on microstrip line with application to antennas," *Radio Sci.*, Vol. 22, 907–912, Nov. 1987.
2. Shigesawa, H., M. Tsuji, and A. A. Oliner, "Conductor-backed slot line and coplanar waveguide: Dangers and full-wave analysis," *Proc. IEEE Int. Microwave Symp. Dig.*, 199–202, June 1988.
3. Michalski, K. A. and D. Zheng, "Rigorous analysis of open microstrip lines of arbitrary cross section in bound and leaky regimes," *IEEE Trans. Microwave Theory and Techniques*, Vol. MTT-37, 2005–2010, Dec. 1989.
4. Das, N. K. and D. M. Pozar, "Full-wave spectral-domain computation of material, radiation, and guided wave losses in infinite multilayered printed transmission lines," *IEEE Trans. Microwave Theory and Techniques*, Vol. MTT-39, 54–63, Jan. 1991.
5. Shigesawa, H., M. Tsuji, and A. A. Oliner,, "Dominant mode power leakage from printed-circuit waveguide," *Radio sci.*, Vol. 26, 559–564, Mar.–Apr. 1991.
6. Grimm, J. M. and D. P. Nyquist, "Spectral analysis considerations relevant to radiation and leaky modes of open-boundary microstrip transmission line," *IEEE Trans. Microwave Theory and Techniques*, Vol. MTT-41, 150–153, Jan. 1993.
7. Nghiem, D., J. T. Williams, D. R. Jackson, and A. A. Oliner, "Proper and improper dominant mode solutions for stripline with an air gap," *Radio Sci.*, Vol. 28, No. 6, 1163–1180, Nov.–Dec. 1993.
8. Mesa, F. and R. Marques,, "Integral representation of spatial Green's function and spectral domain analysis of leaky covered strip-like lines," *IEEE Trans. Microwave Theory and Techniques*, Vol. MTT-43, 828–837, Apr. 1995.
9. Nghiem, D., J. T. Williams, D. R. Jackson, and A. A. Oliner, "Leakage of the dominant mode on stripline with a small air gap,"

IEEE Trans. Microwave Theory and Techniques, Vol. MTT-43, 2549–2556, Nov. 1995.

10. Shigesawa, H., M. Tsuji, and A. A. Oliner, "A simultaneous propagation of bound and leaky dominant modes on printed-circuit lines: A new general effect," *IEEE Trans. Microwave Theory and Techniques*, Vol. MTT-43, 3007–3019, Dec. 1995.
11. Mesa, F. and R. Marques,, "Power based considerations on the spectral domain analysis of leaky waves in covered strip-like transmission lines," *Proc. Inst. Elec. Eng.*, Vol. 143, 25–30, Jan. 1996.
12. Das, N. K., "Methods of suppression or avoidance of parallel-plate power leakage from conductor-backed transmission lines," *IEEE Trans. Microwave Theory and Techniques*, Vol. MTT-44, 169–181, Feb. 1996.
13. Nghiem, D., J. T. Williams, D. R. Jackson, and A. A. Oliner, "Existence of a leaky dominant mode on microstrip line with an isotropic substrate: Theory and measurement," *IEEE Trans. Microwave Theory and Techniques*, Vol. MTT-44, 1710–1715, Oct. 1996.
14. Mesa, F., D. R. Jackson, and M. J. Freire, "Evolution of leaky modes on printed-circuit lines," *IEEE Trans. Microwave Theory and Techniques*, Vol. MTT-50, 94–104, Jan. 2002.
15. Boukamp, J. and R. H. Jansen, "Spectral domain investigation of surface wave excitation and radiation by microstrip lines and microstrip disk resonator," *Proc 13rd European Microwave Conf.*, 721–726, Sept. 1983.
16. Bagby, J. S., C.-H. Lee, D. P. Nyquist, and Y. Yuan, "Identification of propagation regimes on integrated microstrip transmission lines," *IEEE Trans. Microwave Theory and Techniques*, Vol. MTT-41, 1887–1893, Nov. 1993.
17. Shigesawa, H., M. Tsuji, and A. A. Oliner, "The nature of the spectral-gap between bound and leaky solution when dielectric loss is present in printed-circuit lines," *Radio sci.*, Vol. 28, No. 6, 1235–1243, Nov.–Dec. 1993.
18. Cina, J. L. and L. Carin, "Mode conversion and leaky-wave excitation at open-end coupled-microstrip discontinuities," *IEEE Trans. Microwave Theory and Techniques*, Vol. MTT-43, 2066–2071, Sept. 1995.
19. Das, N. K., "Power leakage, characteristic impedance and leakage-transition behaviour of finite-length stub section of leaky printed transmission lines," *IEEE Trans. Microwave Theory and Techniques*, Vol. MTT-44, 526–536, Apr. 1996.

20. Chou, G.-J. and C.-K. C. Tzuang, "Oscillator-type active-integrated antenna: The leaky mode approach," *IEEE Trans. Microwave Theory and Techniques*, Vol. MTT-44, 2265–2272, Dec. 1996.
21. Nallo, C. D., F. Mesa, and D. R. Jackson, "Excitation of leaky modes on multilayer stripline structures," *IEEE Trans. Microwave Theory and Techniques*, Vol. MTT-46, 1062–1071, Aug. 1998.
22. Felsen, L. B. and N. Marcuvitz, *Radiation and Scattering of Waves*, Chapter 5, Prentice-Hall, Englewood Cliffs, N.J., 1973.
23. Collin, R. E., *Field Theory of Guided Waves*, 2nd ed., New York, IEEE Press, 1991.
24. Pozar, *Microwave Engineering*, 185, Addison-Wesley Publishing Company, Inc, 1990.
25. Nallo, C. D., F. Mesa, and D. R. Jackson, "Excitation of leaky modes on multilayer stripline structures," *IEEE Trans. Microwave Theory and Techniques*, Vol. MTT-46, 1062–1071, Aug. 1998.
26. Jackson, D. R., F. Mesa, M. J. Freire, D. P. Nyquist, and C. D. Nallo, "An excitation theory for bound modes, leaky modes, and residual-wave currents on stripline structures," *Radio Sci.*, Vol. 35, 495–510, Mar.–Apr. 2000.
27. Nyquist, D. P., J. M. Grimm, D. J. Infante, and H. Braunisch, "Classification of the proper propagation-mode spectrum and leaky-wave modes on open planar waveguides," *Electromagnetics*, Vol. 17, 105–130, 1997.
28. Chew, W. C., *Waves and Fields in Inhomogeneous Media*, Van Nostrand Reinhold, New York, 1990.
29. Lee, J., "The asymptotic radiation field and proper propagation mode spectra of the open planar waveguide," Ph.D. thesis, Dept. of Elec. and Comp. Eng., Michigan State University, East Lansing, Michigan, 2002.